



A model for focused-beam microwave heating on rock fracturing

Hongwen Yu · Yuanhui Li · Guanglei Cui · Derek Elsworth · Jianpo Liu · Mingfei Liu

Received: 21 December 2020 / Accepted: 14 April 2021 / Published online: 27 April 2021
© The Author(s), under exclusive licence to Springer Nature Switzerland AG 2021

Abstract Microwave-assisted rock fracturing has been widely applied to satisfy increasing demands for safety, high efficiency and energy saving. During microwave irradiation, rock damage occurs as a result of the irregular distribution of induced temperatures and resulting thermal stresses. This non-uniform temperature distribution may develop from either (1) intrinsic rock heterogeneity, or (2) from the impingement of a heterogeneous or focused electromagnetic field density. However, prior models have rarely been concerned with the impact of the latter phenomenon and no rational methods to define the accurate location of the initial fracturing are available. A nested spherical mechanical model is proposed to address this deficiency where the heated volume is divided into three zones: an interior high temperature zone (H zone), a transition zone (T zone) and a low temperature external zone (L zone). The thermal stress coupling coefficient is defined. The proposed model is verified against experiments conducted in this work and by others. As a result of this mechanical model, the

geometric dimensions of the three regions have an important influence on the variation of the maximum compressive/tensile stress. The thermal stress coupling coefficient is closely related to the location of the maximum compressive/tensile stress and the thermal stress distribution. Fractures develop first in the extensional T zone. The proposed model enables the prediction of the likelihood, location and severity of fracturing to develop and therefore enables the potential optimization of the fracturing process.

Article Highlights

- We develop a nested spherical mechanical model to address this deficiency where the heated volume is divided into three zones: H zone, T zone and L zone.
- The stress distribution is shown to be uniquely related to both the thermal stress coupling coefficients and the geometric dimensions of the three zones.
- The maximum tensile stress appears in the inner boundary of T zone, or a small distance from H zone.

Keywords Microwave heating · Non-uniform temperature distribution · Thermal expansion · Temperature gradient · Coupling coefficient

H. Yu · Y. Li (✉) · G. Cui · J. Liu · M. Liu
Key Laboratory of Ministry of Education on Safe Mining
of Deep Metal Mines, Northeastern University,
Shenyang 110819, China
e-mail: neulyh@163.com

D. Elsworth
Department of Energy and Mineral Engineering, G3
Center and Energy Institute, The Pennsylvania State
University, University Park, PA 16802, USA

1 Introduction

Microwave-assisted fracturing has been widely applied in the breaking (Satish et al. 2006), fracturing (GUO et al. 2011; Wen et al. 2017) and the processing (Buttress et al. 2017; Amankwah and Pickles 2009) of various rocks. Additionally, microwave heating can be used not only in the comminution of minerals but in tunnel engineering, mining engineering and in the recovery of unconventional reservoirs (Hartlieb et al. 2018; Li et al. 2019a; Liu et al. 2018). Numerous experiments and theoretical models have been developed to assess mechanisms of damage resulting from microwave irradiation (Jones et al. 2007; Li et al. 2019b). These studies have principally focused on the thermodynamic mechanisms underpinning damage, fracturing modes at a micro scale, and the patterns of induced fractures at macro scale.

These studies have revealed that microwave-induced fractures are mainly radial (Meisels et al. 2015). In terms of microscopic fracturing, rocks are mainly subjected to intergranular failure with some transgranular breakage (Charikinya et al. 2015; Omran et al. 2015). The applied microwave power, the irradiation time, and the mineral constitutes importantly influence the heating degrees of rocks irradiated with the microwave energy (Kahraman et al. 2020), and mineral size and spatial distribution on the damage caused by microwave irradiation (Li et al. 2019b). Such models identify general trends in response that note: (1) For the same input microwave energy, the higher the microwave power, the greater the damage (Jones et al. 2007; Rizmanoski 2011); (2) For given microwave power, the longer the duration of irradiation, the greater the damage (Li et al. 2019b, 2016; Kingman et al. 2004), although for a given mineralogy and ore structure there is a minimum threshold power density below which no damage at grain boundaries results, regardless of the duration of exposure (Ali and Bradshaw 2009); (3) An optimal combination of power and duration of exposure exists for irradiation at a specified microwave energy (Zheng et al. 2017); (4) Exposure at a given microwave power and input microwave energy preferentially damages larger particles of absorbing minerals (Jones et al. 2005).

A non-uniform temperature field is generated during microwave irradiation, thus generating thermal stress and initiating damage (Li et al. 2019b; Toifl et al. 2017). Non-uniform temperatures result from

both the anisotropic and heterogeneous properties of mineral aggregates and the heterogeneous distribution of heating resulting from the focus of the microwave beam. Different mineral aggregates exhibit different absorptive capacities to microwaves (Jones et al. 2007; Toifl et al. 2017; Pitchai et al. 2014; Zhang et al. 2016). The dielectric properties of minerals were then used to explain the behavior difference minerals when exposed to microwave radiation (Zheng et al. 2020). Thus, the non-uniformity of these properties, and hence selective absorption by material aggregates, is one of the keys to increasing the aforementioned damage (Meisels et al. 2015). Furthermore, microwave intensity is typically non-uniform in the area heated by the radiation (Hartlieb et al. 2016; Hartlieb and Grafe 2017; Lu et al. 2019)—as a result of beam focusing. This is the main reason for the development of a non-uniform temperature distribution in quasi-homogeneous materials.

Microwave heating-induced fracturing usually occurs at the boundary between high temperature and low temperature areas (Hong et al. 2016). Mechanisms of microwave-induced rock fracturing illuminated in previous work have been represented in numerical models of non-equilibrium thermodynamics accommodating two complementary processes: (1) thermal stresses induced by the temperature gradient between high temperature area and low temperature areas (Jones et al. 2005; Toifl et al. 2017; Hartlieb et al. 2012; Yan and Zheng 2017); and (2) thermal stresses generated by mechanical restraint of a heated core by a surrounding lower temperature collar (Hartlieb et al. 2016; Wang and Djordjevic 2014). The former identifies local stress gradients and the latter the overall magnitudes of the stresses, and their respective impact on generating fractures. These combined effects induce tensile stresses in the peripheral matrix and shear stress at the boundary between the two different areas. The rock is damaged as strains/stresses exceed a threshold strain/strength (Hartlieb et al. 2012). Typical observations indicate that microwave-heating-induced fractures are concentrated at the interface between areas of contrasting temperatures (Hong et al. 2016) with some studies contending that fracturing initiates some distance from that boundary (Wang and Djordjevic 2014). Mechanisms contributing to fracture initiation at the boundary are well defined while those remote from the boundary are not—and indeed remain poorly understood. In

addition, most studies have focused on the impacts of the non-uniform temperature/stress distribution caused by the anisotropic and heterogeneous nature of the energy-adsorptive and thermomechanical properties of mineral aggregates—with few studies exploring the impact of the heterogeneous distribution of microwave intensity. This is despite this latter feature being commonly observed in quasi-homogeneous rocks such as basalts and granites (Meisels et al. 2015) where the initial appearance of fracture appears mainly related to the temperature gradient (Toifl et al. 2017, 2016; Hartlieb et al. 2012) with little relation to the type of mineral aggregate (Hartlieb et al. 2012).

To summarize, current studies constraining the precise location of damage and fracture in quasi-homogeneous materials, where the impact of focused and uneven microwave intensity is present, are rare. Ignoring this effect potentially results in the misclassification of fracture—both in intensity and location—that will result from microwave irradiation where focusing is strong. The following addresses this deficiency by defining both thermal and thermally-induced-stress-profiles that result from the thermomechanical loading of a focused microwave beam into a quasi-homogeneous medium. This model is used to define the location and intensity of the resulting microwave heating-induced fracturing. The model is applied to understand contrasting mechanisms controlling the initiation of fracture in both heterogeneous rocks and for uneven distribution of microwave radiation intensity. The model accommodates a central high temperature (irradiated) zone encased within a low temperature zone and linked by an intermediate thermal transition zone. Thermal stresses resulting from this spherically symmetric heating regime are analyzed to define the location and pattern of the microwave heating-induced fracturing and thereby discriminate between various causal mechanisms for damage evolution.

2 Nested spherical mechanical model

2.1 Model assumptions

Prior to microwave heating the rock is at equilibrium in both stress and temperature, with stress and temperature identically uniform. Post heating, temperatures and induced thermal stresses are non-

uniform due to either the nested heterogeneity of the adsorptive/thermomechanical properties of the mineral aggregates (adsorptive mineral in a non-adsorptive matrix host) or the heterogeneous distribution of microwave intensity (applied to a uniformly adsorptive medium). The system is divided into three concentrically spherical zones—an interior high temperature zone (H), an exterior low temperature zone (L) and transition zone (T) between them, as shown in Fig. 1. The low-temperature L Zone remains at ambient temperature since it is beyond the influence of the focused microwave beam. The high-temperature H Zone results from rapid heating by the focused beam within its area of impingement. And the equilibrium temperature across the transitional T Zone transitions between the bounding temperatures on either side ($T_H > T_T > T_L$). Thus, a significant temperature gradient develops across this smeared interface (T Zone) separating the H and L Zones (Fig. 1). Three major assumptions are made to simplify the system, while honoring the principal mechanisms for stress generation: (1) the temperatures gradient in the H and L Zones is small and can be ignored, in other words temperature gradients within the H and L Zones are identically zero; and (2) the three zones are fully bonded, with no slip and separation or fracturing between each zone, and (3) the dynamic heat transfer process of microwave radiation is assumed to be composed of a quasi-static steady process. The temperature distribution in T zone is related to the temperature in H zone and the radius of T zone.

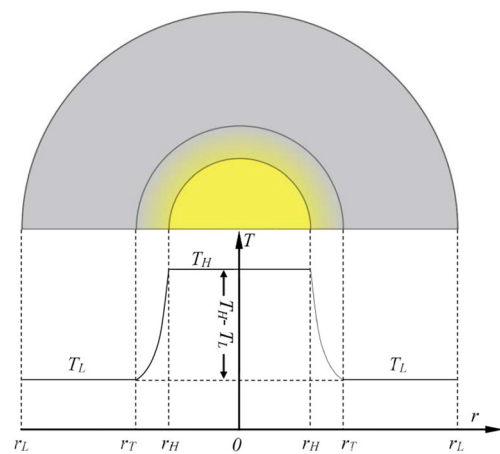


Fig. 1 Schematic of uniform temperature distributions within high (irradiated) and low (ambient) temperature zones, linked by the thermal gradient in the transitional zone

An identical model can be used to represent (1) a small microwave adsorptive mineral embedded within a non-adsorptive host or (2) a narrowly focused microwave beam impinging on a uniformly adsorptive material. For either of these cases it is assumed separately that (1) the content of microwave adsorptive mineral grain is much smaller than the surrounding non-adsorptive mineral (Jones et al. 2007) or that (2) the microwave focus is narrow in comparison to the external region. In each of these cases [(1) and (2)] $r_L \gg r_T > r_H$. The relationships describing steady state temperatures in the H, L, and T zones subject of irradiation are (Li et al. 2019a, b; Pitchai et al. 2014; Zhang et al. 2016):

$$T_H = f_H(t, \kappa_H, C_{pH}, \mathbf{E}_H, \lambda_H) \tag{1}$$

$$T_L = f_L(t, \kappa_{T\&L}, C_{pT\&L}, \mathbf{E}_{T\&L}, \lambda_{T\&L}) \tag{2}$$

$$T_{Tr} = \frac{C_1}{r} + C_2 \tag{3}$$

in which,

$$C_1 = \frac{T_H - T_L}{1/r_H - 1/r_T}, \quad C_2 = T_H - \frac{T_H - T_L}{r_H(1/r_H - 1/r_T)} \tag{4}$$

where T represents the temperature, r represents radius from the center of focus (or center of adsorptive mineral) and subscripts H , T and L represent the H, T and L Zones; t , κ , C_p , \mathbf{E} , and λ represent time, permittivity, specific heat capacity, electric field intensity and thermal conduction coefficient.

Based on the definition of the three zones, the boundaries of H-T and T-L zones can be defined by the changing of temperature gradient. In the experiment, the infrared thermograph is applied to obtain the temperature distribution of rock surface. Next, the temperature contour map of rock surface is calculated with the temperature gradient obtained. The area where the temperature gradient larger than 5% of the maximum temperature gradient is defined as T zone. The boundaries of H-T and T-L zones are located at the position where the temperature gradient is 5% of the maximum temperature gradient. The boundary with high temperature is defined as boundary of H-T Zone and the other is specified as boundary of L-T Zone.

2.2 Stress analysis

In the following, we consider the thermal stresses generated by microwave irradiation as partitioned into two components: the stresses induced by thermal expansion in the heated zone, comprising a uniform induced temperature, and that triggered by the temperature gradient in the T zone, where stress continuity is enforced and the induced stresses vary with radius. In this section, the stress conditions within each zone are defined and the results superposed to define the resulting stress distribution—but more importantly, do define the impacts of different factors in describing the stress distribution, sense (tensile or compressional) and intensity.

The stress distribution within the H zone is first defined. For this, the T and L Zones are combined and labeled as the T&L Zone, for simplicity. Since H Zone is in close contact with, and surrounded by the T&L Zone, the thermal expansion of the H Zone is restricted and a pressure ($P_{H-T\&L}$) is generated at the contact (Fig. 2) and labeled as $P_{Ho(H-T\&L)}$ on the outer boundary of the H Zone and $P_{T\&Li(H-T\&L)}$ on the inner boundary of the T & L Zone with $P_{Ho(H-T\&L)} = P_{T\&Li(H-T\&L)}$. As a result of this stress transfer, $P_{T\&Li(H-T\&L)}$ acts across the entire area of the T&L Zone. In the definition of variables used in this paper, capital letters H, T, and L represent the H, T and L Zones, and the lowercase letters o and i represent the outer and inner boundaries of each zone.

The T Zone expands as a result of the temperature gradient. Due to the constraint of the L Zone, stress is generated on both the outer boundary of the T Zone and the inner boundary of the L Zone, labelled as $P_{To(T-L)}$ and $P_{Li(T-L)}$ with $P_{To(T-L)} = P_{Li(T-L)}$. The T Zone expands inside due to the temperature gradient. However, the inner boundary of T Zone also expands as a result of the temperature gradient and the impact of $P_{Li(T-L)}$. Similarly due to the constraint of the H Zone, pressures are generated on both the outer boundary of the H Zone and the inner boundary of T & L Zone, labelled as $P_{Ho(T\&L-H)}$ and $P_{T\&Li(T\&L-H)}$. Also, $P_{T\&Li(T\&L-H)}$ acts across the entire area of the T&L Zone. Later we will demonstrate that both values of $P_{Ho(T\&L-H)}$ and $P_{T\&Li(T\&L-H)}$ are equal to zero. The temperature increment in the L Zone is small compared with that in the H and T Zones. Therefore, the thermal stress induced by the L Zone is taken as zero.

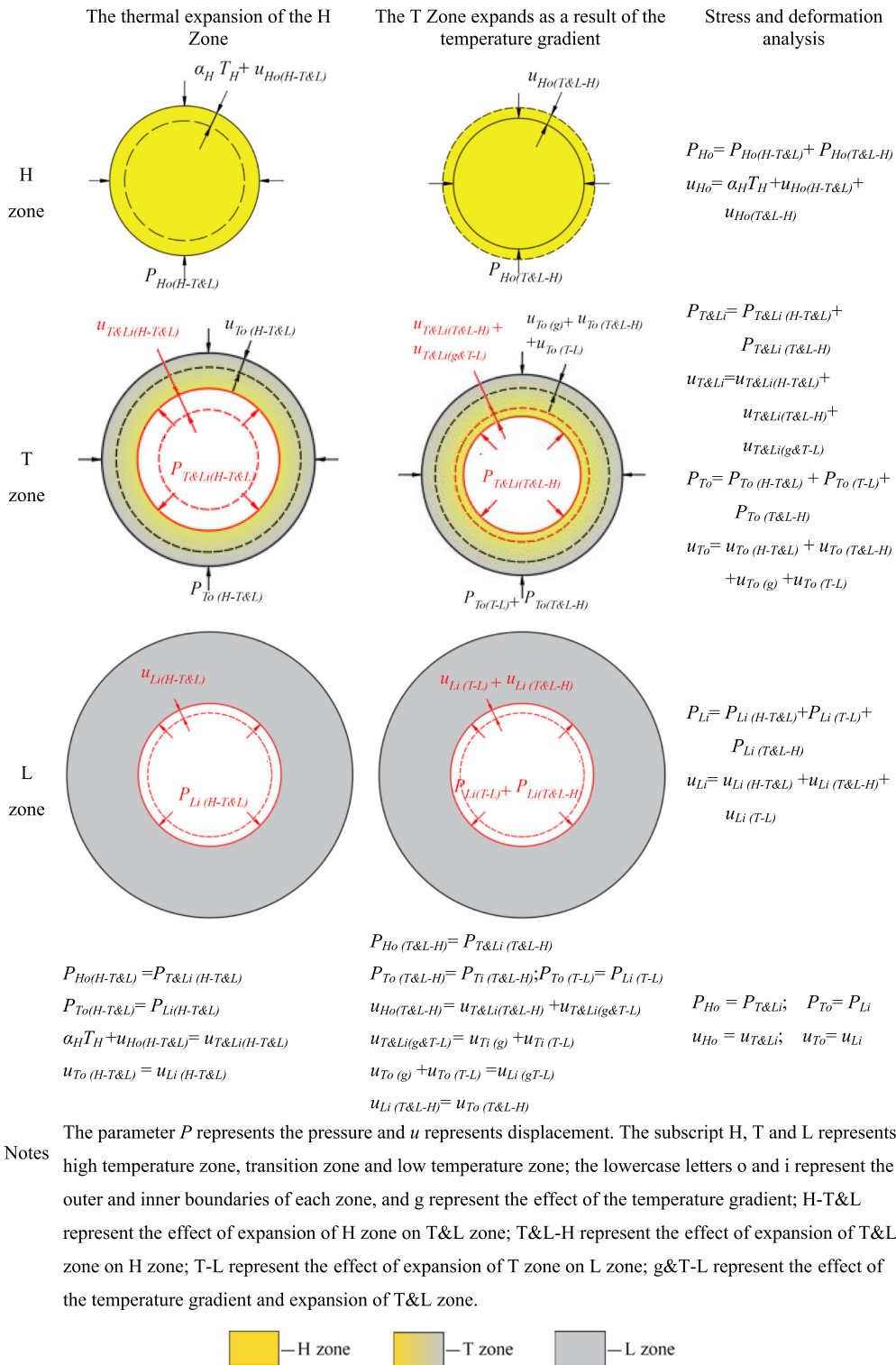


Fig. 2 Stress and deformation analysis to the interfaces within the model, the dotted line in the figure represents the original boundary and the solid line represents the microwaved boundary; the red circle is the inner boundary and the black circle is the outer boundary

(1) Stress Analysis on the contact surface between the H and T&L Zones

Based on the previous analysis, we obtain the pressure applied on the contact surface between H and T&L Zones, as:

$$P_{Ho} = P_{Ho(H-T\&L)} + P_{Ho(T\&L-H)} \tag{5}$$

$$P_{T\&Li} = P_{T\&Li(H-T\&L)} + P_{T\&Li(T\&L-H)} \tag{6}$$

in which P_{Ho} and $P_{T\&Li}$ are the resultant pressures of the outer boundary of the H Zone and the inter boundary of the T&L Zone, with $P_{Ho} = P_{T\&Li}$.

(2) Stress Analysis on the contact surface between the T and L Zones

The stress states of the T and L Zones are presented here. Similarly the thermal expansion generates an interaction pressure on the interface between the the T and L zones, as $P_{To(T-L)}$ and $P_{Ti(T-L)}$. Furthermore, $P_{T\&Li(H-T\&L)}$ generates pressure on outer boundary of the T Zone and the inner boundary of the L Zone, identified as $P_{To(H-T\&L)}$ and $P_{Li(H-T\&L)}$. Similarly, $P_{T\&Li(T\&L-H)}$ generates pressures on outer boundary of the T Zone and the inner boundary of the L Zone, labelled as $P_{To(T\&L-H)}$ and $P_{Ti(T\&L-H)}$. Allowing us to obtain:

$$P_{To} = P_{To(H-T\&L)} + P_{To(T\&L-H)} + P_{To(T-L)} \tag{7}$$

$$P_{Li} = P_{Li(H-T\&L)} + P_{Li(T\&L-H)} + P_{Li(T-L)} \tag{8}$$

where P_{To} represents the resultant pressure on the outer interface of the L zone; and P_{Li} represents the resultant pressure on the inner interface of the L zone. Furthermore, the pressure applied on the outer boundary of the T Zone due to the thermal expansion of the H Zone is the same as that on the inner boundary of the L zone. Therefore we have: $P_{To(H-T\&L)} = P_{Li(H-T\&L)}$ and $P_{To(T\&L-H)} = P_{Ti(T\&L-H)}$.

(3) Deformation at the interface between the H Zones and T&L Zones

The displacement of at the interface between the H Zone and the T Zone is first analyzed. The outward displacement of the H Zone (u_{Ho}) is equal to the sum of the free expansion of the H Zone under uniform heat expansion and the synergistic displacement under the effects of $P_{Ho(H-T\&L)}$ and $P_{Ho(T\&L-H)}$. The displacement on the inner boundary of the T&L Zone ($u_{T\&Li}$) is

the superposition of the displacement induced by the thermal gradient and $P_{Ti(T-L)}$, the displacement due to $P_{T\&Li(H-T\&L)}$ and the displacement induced by $P_{T\&Li(T\&L-H)}$. The inward displacement of the T&L Zone ($u_{T\&Li}$) is equivalent to the sum of the free expansion of the T Zone under thermal expansion and the synergistic displacement under the effects of $P_{Ti(T-L)}$ and $P_{T\&Li(T\&L-H)}$. Under the assumption that the H zone and T Zone are bonded, then $u_{Ho} = u_{Ti}$. Therefore we have:

$$r_H \alpha_H T_H + u_{Ho(H-T\&L)} + u_{Ho(T\&L-H)} = u_{T\&Li(H-T\&L)} + u_{T\&Li(T\&L-H)} + u_{T\&Li(g\&T-L)} \tag{9}$$

where the first term represents the free expansion of the H Zone induced displacements, where $u_{Ho(H-T\&L)}$ and $u_{Ho(T\&L-H)}$ represent the $P_{Ho(H-T\&L)}$ and $P_{Ho(T\&L-H)}$ induced displacement on the outer boundary of the H Zone; $u_{T\&Li(H-T\&L)}$ and $u_{T\&Li(T\&L-H)}$ represent the $P_{T\&Li(H-T\&L)}$ and $P_{T\&Li(T\&L-H)}$ induced displacement on the inner boundary of the T&L zone; $u_{T\&Li(g\&T-L)}$ represents the temperature gradient and $P_{Ti(T-L)}$ induced displacement on the inner boundary of the T&L zone. Then we obtain:

$$u_{T\&Li(g\&T-L)} = u_{Ti(g)} + u_{Ti(T-L)} \tag{10}$$

where $u_{Ti(T-L)}$ represents the displacement on the inner boundary of the T Zone induced by $P_{Ti(T-L)}$; and $u_{Ti(g)}$ represents the displacement on the inner boundary of T Zone induced by temperature gradient.

(4) Deformation at the interface between the T and L Zones

Now the displacement of the interface between the T Zone and the L Zone is investigated. The displacement of the outer boundary in the T zone (u_{To}) is equal to the sum of that induced by compressive stress of the H Zone and the interaction with the temperature gradient of the L zone. The displacement of the inner boundary of the L zone (u_{Li}) is caused by the compressive stress of the H Zone and interaction with the L zone. Also we have $u_{To} = u_{Li}$ and:

$$u_{To(g)} + u_{To(T-L)} + u_{To(H-T\&L)} + u_{To(T\&L-H)} = u_{Li(T-L)} + u_{Li(H-T\&L)} + u_{Li(T\&L-H)} \tag{11}$$

where $u_{To(g)}$ represents the displacement on the outer boundary of the T Zone induced by temperature gradient; $u_{To(T-L)}$ represents the $P_{To(T-L)}$ induced displacement on the outer boundary of the T Zone; and

$u_{Li(T-L)}$ denotes the $P_{Li(T-L)}$ induced displacement on the inner boundary of the L Zone. $u_{To(H-T&L)}$ and $u_{Li(H-T&L)}$ represent the $P_{T&Li(H-T&L)}$ induced displacements on the outer boundary of the T Zone and the inter boundary of the L Zone; $u_{To(T&L-H)}$ and $u_{Li(T&L-H)}$ represent the $P_{T&Li(T&L-H)}$ induced displacement on the outer boundary of the T Zone and the inter boundary of the L Zone.

Also, the displacement on the outer boundary of the T Zone due to the thermal expansion of the H Zone is the same as that on the inner boundary of the L zone, therefore we have $u_{To(H-T&L)} = u_{Li(H-T&L)}$, $u_{To(T&L-H)} = u_{Li(T&L-H)}$ and:

$$u_{To(g)} + u_{To(T-L)} = u_{Li(T-L)} \tag{12}$$

inner pressure applied on a hollow sphere with an inner radius of r_T and outer radius of r_L . The temperature gradient will also generate a thermal stress in the T Zone as noted in ‘‘Temperature gradient induced stress within a hollow sphere’’ section in ‘‘Appendix 1’’. The inner stress in the H Zone is induced by $P_{Ho(H-T&L)}$ and $P_{Ho(T&L-H)}$, the inner stress inside the T Zone is induced by the combination of temperature gradient in the T Zone, $P_{T&Li(H-T&L)}$, $P_{T&Li(T&L-H)}$ and $P_{To(T-L)}$; The inner stress inside the L Zone is induced by $P_{T&Li(H-T&L)}$, $P_{T&Li(T&L-H)}$ and $P_{Li(T-L)}$.

Therefore, we can obtain the radial and circumferential stress in each zone:

$$\sigma_r = \begin{cases} -\frac{2\alpha_H E_H E_{T\&L} T_H}{(1 + \mu_{T\&L}) E_H + 2(1 - 2\mu_H) E_{T\&L}} & (0 < r \leq r_H) \\ \frac{\alpha_{T\&L} E_{T\&L} T_H}{(1 - \mu_{T\&L})(r_T - r_H)} \left[\frac{2r_H}{3} - \frac{r_H r_T}{r} + \frac{r_H^3(3r_T - 2r_H)}{3r^3} \right] - \frac{2\alpha_H E_H E_{T\&L} T_H r_H^3}{[(1 + \mu_{T\&L}) E_H + 2(1 - 2\mu_H)] E_{T\&L} r^3} & (r_H \leq r \leq r_T) \\ -\frac{\alpha_{T\&L} E_{T\&L} T_H r_H (r_T - r_H)(2r_H + r_T)}{3(1 - \mu_{T\&L}) r^3} - \frac{2\alpha_H E_H E_{T\&L} T_H r_H^3}{[(1 + \mu_{T\&L}) E_H + 2(1 - 2\mu_H)] E_{T\&L} r^3} & (r_T \leq r \leq r_L) \end{cases} \tag{13}$$

$$\sigma_\theta = \begin{cases} -\frac{2\alpha_H E_H E_{T\&L} T_H}{(1 + \mu_{T\&L}) E_H + 2(1 - 2\mu_H) E_{T\&L}} & (0 < r \leq r_H) \\ \frac{\alpha_{T\&L} E_{T\&L} T_H}{(1 - \mu_{T\&L})(r_T - r_H)} \left[\frac{2r_H}{3} - \frac{r_H r_T}{2r} - \frac{r_H^3(3r_T - 2r_H)}{6r^3} \right] + \frac{\alpha_H E_H E_{T\&L} T_H r_H^3}{[(1 + \mu_{T\&L}) E_H + 2(1 - 2\mu_H)] E_{T\&L} r^3} & (r_H \leq r \leq r_T) \\ \frac{\alpha_{T\&L} E_{T\&L} T_H r_H (r_T - r_H)(2r_H + r_T)}{6(1 - \mu_{T\&L}) r^3} + \frac{\alpha_H E_H E_{T\&L} T_H r_H^3}{[(1 + \mu_{T\&L}) E_H + 2(1 - 2\mu_H)] E_{T\&L} r^3} & (r_T \leq r \leq r_L) \end{cases} \tag{14}$$

2.3 Mechanical model

In this section, a mechanical model is established based on the solutions to several scenarios for the thermoelastic problem listed in ‘‘Appendix 1’’. The action of $P_{Ho(H-T&L)}$ on the H zone can be treated as an outer pressure applied on a solid sphere with a radius of r_H . The action of $P_{Ti(H-T&L)}$ and $P_{To(T-L)}$ can be treated as inner and outer pressures applied on a hollow sphere with the inner radius of r_H and outer radius of r_T . The action of $P_{Li(T-L)}$ can be treated as an

where α_H , $\lambda_{T\&L}$, E_H , $E_{T\&L}$, μ_H , and $\mu_{T\&L}$ refer to the coefficients of thermal expansion, Young’s moduli, and Poisson’s ratios of the H and T&L zones; r_H , r_T , and r_L denote the radii of the H, T, and L zones; σ_r and σ_θ represent the radial and circumferential stresses, respectively.

Based on Eqs. (13) and (14), the radial stress and circumferential stress are both related to the thermal expansion and temperature gradient. For simplicity we define the temperature gradient stress coupling coefficient (n) and thermal expansion stress coupling coefficient (m) as:

$$n = \frac{\alpha_{T\&L} E_{T\&L} T_H}{(1 - \mu_{T\&L})} \tag{15}$$

$$m = \frac{3\alpha_H E_H E_{T\&L} T_H}{(1 + \mu_{T\&L}) E_H + 2(1 - 2\mu_H) E_{T\&L}} \tag{16}$$

Therefore with the substitution of Eqs. (15) and (16) into Eqs. (13) and (14), the above equations can be written as:

$$\sigma_r = \begin{cases} -\frac{2m}{3} & (0 < r \leq r_H) \\ \frac{n}{(r_T - r_H)} \left[\frac{2r_H}{3} - \frac{r_H r_T}{r} + \frac{r_H^3 (3r_T - 2r_H)}{3r^3} \right] - \frac{2mr_H^3}{3r^3} & (r_H \leq r \leq r_T) \\ \frac{n r_H (r_T - r_H) (2r_H + r_T)}{3r^3} - \frac{2mr_H^3}{3r^3} & (r_T \leq r \leq r_L) \end{cases} \tag{17}$$

$$\sigma_\theta = \begin{cases} -\frac{2m}{3} & (0 < r \leq r_H) \\ \frac{n}{(r_T - r_H)} \left[\frac{2r_H}{3} - \frac{r_H r_T}{2r} - \frac{r_H^3 (3r_T - 2r_H)}{6r^3} \right] + \frac{mr_H^3}{3r^3} & (r_H \leq r \leq r_T) \\ \frac{nr_H (r_T - r_H) (2r_H + r_T)}{6r^3} + \frac{mr_H^3}{3r^3} & (r_T \leq r \leq r_L) \end{cases} \tag{18}$$

3 Evolution of thermal stress during microwave irradiation

In this section, the variation and characteristic of the thermal stress in each zone are illustrated. Four cases are defined based on the relationship of m and n .

3.1 Case I-thermal expansion induced stress dominant

Under the assumption that (1) $\alpha_{T\&L}/\alpha_H \approx 0$ and $n/m \approx 0$, (2) $\lambda_{T\&L}$ is small and no T zone appears, the thermal expansion induced stress is several orders of magnitude greater than the thermal gradient induced stress and the later term can be ignored. Then we have:

$$\sigma_r = \begin{cases} -\frac{2m}{3} & (0 < r \leq r_H) \\ -\frac{2mr_H^3}{3r^3} & (r_H \leq r \leq r_L) \end{cases} \tag{19}$$

$$\sigma_\theta = \begin{cases} -\frac{2m}{3} & (0 < r \leq r_H) \\ \frac{mr_H^3}{3r^3} & (r_H \leq r \leq r_L) \end{cases} \tag{20}$$

As shown in Fig. 3a, all radial stresses are compressive, and are uniformly distributed in the H zone, while they decrease with increasing radius in the T&L zone. The maximum compressive stress appears in the H zone, and its magnitude is independent of r and r_H .

As shown in Fig. 3b, the tangential stress in the H zone is uniformly distributed and compressive. In the T&L zone, the tangential stresses are tensile and decrease with increasing radius. At the boundary of the T zone, the maximum tensile stress is half the maximum compressive stress. We therefore conclude that compression-induced damage is likely to occur in the H zone and tensile induced damage would first appear at the interface between the H and T zones with potential extension into the L zone.

3.2 Case II-temperature gradient induced stress dominant

Under the assumption that (1) $\alpha_H \approx 0$ therefore $m \approx 0$, (2) αT_H is small and $(T_H - T_L)/(r_T - r_H)$ is sufficiently large to guarantee that the temperature gradient-induced stress is several orders of magnitude greater than the thermal expansion-induced stress then the latter term can be ignored. We obtain the following equation:

$$\sigma_r = \begin{cases} 0 & (0 < r \leq r_H) \\ \frac{n}{(r_T - r_H)} \left[\frac{2r_H}{3} - \frac{r_H r_T}{r} + \frac{r_H^3 (3r_T - 2r_H)}{3r^3} \right] & (r_H \leq r \leq r_T) \\ -\frac{n}{3(1 - \mu)} \frac{r_H (r_T - r_H) (2r_H + r_T)}{r^3} & (r_T \leq r \leq r_L) \end{cases} \tag{21}$$

$$\sigma_\theta = \begin{cases} 0 & (0 < r \leq r_H) \\ \frac{n}{(r_T - r_H)} \left[\frac{2r_H}{3} - \frac{r_H r_T}{2r} - \frac{r_H^3 (3r_T - 2r_H)}{6r^3} \right] & (r_H \leq r \leq r_T) \\ \frac{nr_H (r_T - r_H) (2r_H + r_T)}{6r^3} & (r_T \leq r \leq r_L) \end{cases} \tag{22}$$

3.2.1 Variation of Radial Stress for Case II

As shown in Fig. 4a, the maximum value of compressive stress appears in the T zone, and the radial stresses in the T and the L zones are both compressive with the absolute value first increasing, then decreasing with increasing radius. To identify the location of the maximum value of compressive stress, the radial

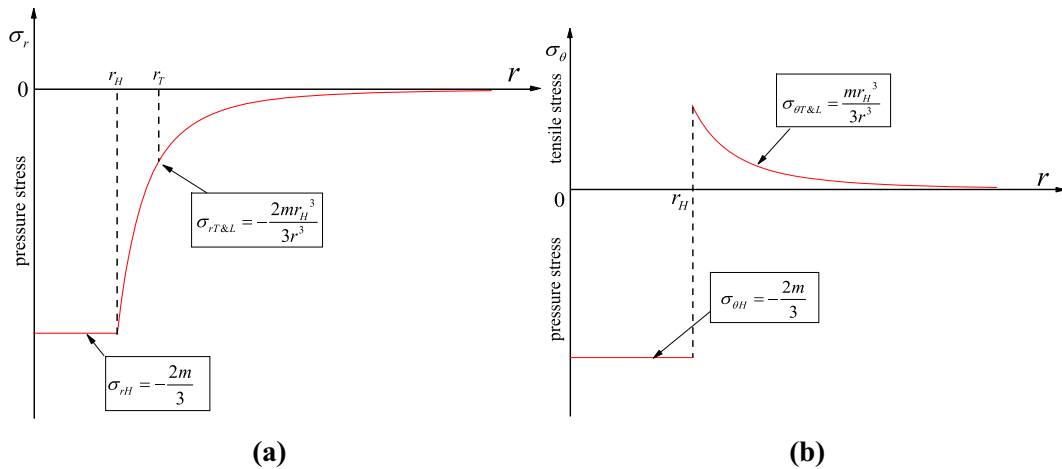


Fig. 3 Variation of **a** σ_r and **b** σ_θ with radius for Case I. Subscript r represents the radial stress and θ represents the circumferential stress. H, L, and T represent the high (H Zone)

and low (L Zone) temperature zones with the transitional (T Zone) temperature zone linking them

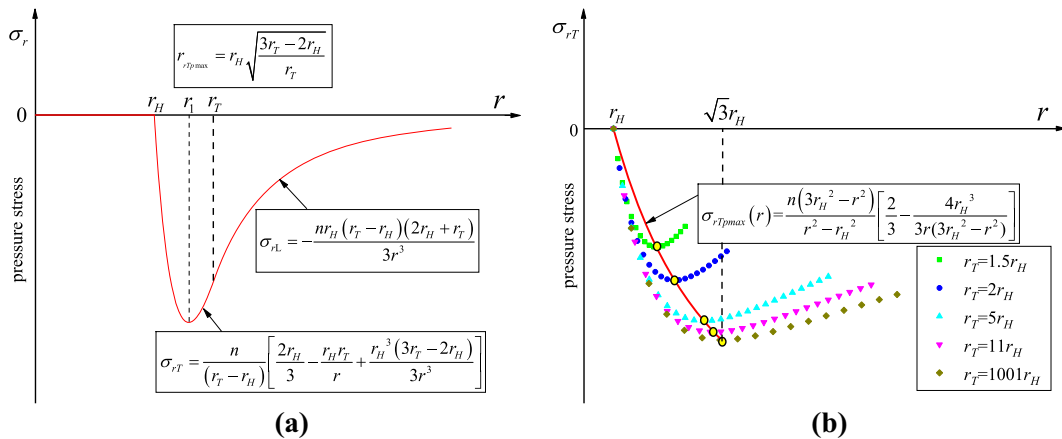


Fig. 4 Variation of **a** σ_r with radius r and **b** σ_r with radius r for different r_T/r_H and σ_{rTpmax} for Case II

derivative of Eq. (21) is applied and set to zero. Thus, we obtain:

$$r_{rTpmax} = r_H \sqrt{\frac{3r_T - 2r_H}{r_T}} \tag{23}$$

$$\sigma_{rTpmax}(r) = \frac{n(3r_H^2 - r^2)}{r^2 - r_H^2} \left[\frac{2}{3} - \frac{4r_H^3}{3r(3r_H^2 - r^2)} \right] \tag{24}$$

where σ_{rTpmax} represent the maximum value of the radial stress and r_{rTpmax} represents the location of σ_{rTpmax} .

The variation of σ_{rTpmax} with radius is illustrated in Fig. 4b. The maximum value of σ_{rTpmax} first increases, then eventually stabilizes with an increase in r_T/r_H and

the location of the position of maximum stress shifts outwards to $\sqrt{3}r_H$ with the expansion of the T zone ($r_T/r_H \rightarrow \infty$).

3.2.2 Variation of circumferential stress for Case II

As shown in Fig. 5a, the tangential stress in the T zone transforms from compressive to tensile stress with increasing radius. The tangential stress in the L zone is tensile and decreases with radius. The maximum compressive stress occurs at the inner boundary of the T zone and is invariant with r , r_H , or r_T , but is related to the temperature gradient coupling coefficient (n). The maximum tensile stress occurs at the outer boundary

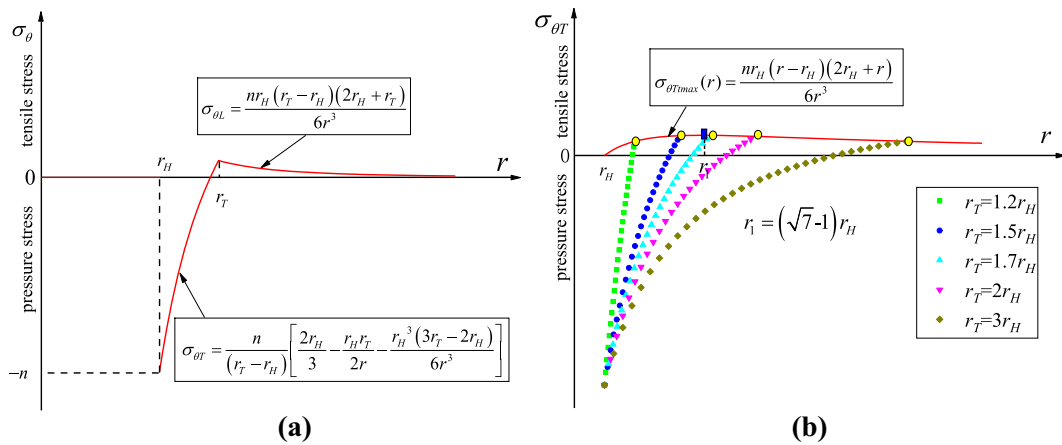


Fig. 5 Variation of **a** σ_θ with radius r and **b** σ_θ with radius r for different r_T/r_H and $\sigma_{\theta Tmax}$ for Case II

of the T zone. Therefore, tensile stress-induced damage would appear at the outer boundary of the T zone and expand both inwards and outwards.

Further, we can obtain the value of $\sigma_{\theta Tmax}$ and the location of its maximum value as:

$$\sigma_{\theta Tmax}(r) = \frac{nr_H(r-r_H)(2r_H+r)}{6r^3} \tag{25}$$

$$r_{\theta Tmax} = r_T = (\sqrt{7}-1)r_H \tag{26}$$

$\sigma_{\theta Tmax}$ represents the maximum values of tangential stress, $r_{\theta Tmax}$ represents the location of the maximum value of $\sigma_{\theta Tmax}$. As shown in in Fig. 5b, the location of the maximum tensile stress shifts outwards with increasing r_T/r_H , with the maximum value first increasing, reaching a peak at $r_{\theta Tmax}=(\sqrt{7}-1)r_H$, then decreasing.

3.3 Case III-thermal expansion and temperature gradient induced stresses equivalent ($m = n$)

Another special case is where the contributions of thermal expansion-induced and temperature gradient-induced stresses are almost equal ($m = n$). This case can result when: (1) the rock can be treated as homogeneous medium and (2) the non-uniform temperature distribution is mainly induced by the heterogeneity of the microwave density. The model can be simplified to:

$$\sigma_r = \begin{cases} -\frac{2m}{3} & (0 < r \leq r_H) \\ \frac{m}{(r_T-r_H)} \left[\frac{2r_H}{3} - \frac{r_H r_T}{r} + \frac{r_H^3(3r_T-2r_H)}{3r^3} \right] - \frac{2mr_H^3}{3r^3} & (r_H \leq r \leq r_T) \\ -\frac{m}{3(1-\mu)} - \frac{r_H(r_T-r_H)(2r_H+r)}{r^3} - \frac{2mr_H^3}{3r^3} & (r_T \leq r \leq r_L) \end{cases} \tag{27}$$

$$\sigma_\theta = \begin{cases} -\frac{2m}{3} & (0 < r \leq r_H) \\ \frac{m}{(r_T-r_H)} \left[\frac{2r_H}{3} - \frac{ar_T}{2r} - \frac{r_H^3(3r_T-2r_H)}{6r^3} \right] + \frac{mr_H^3}{3r^3} & (r_H \leq r \leq r_T) \\ \frac{mr_H(r_T-r_H)(2r_H+r)}{6r^3} + \frac{mr_H^3}{3r^3} & (r_T \leq r \leq r_L) \end{cases} \tag{28}$$

3.3.1 Variation of radial stress for Case III

As shown in Fig. 6, all radial stresses are compressive. The compressive stress within the H zone is uniformly

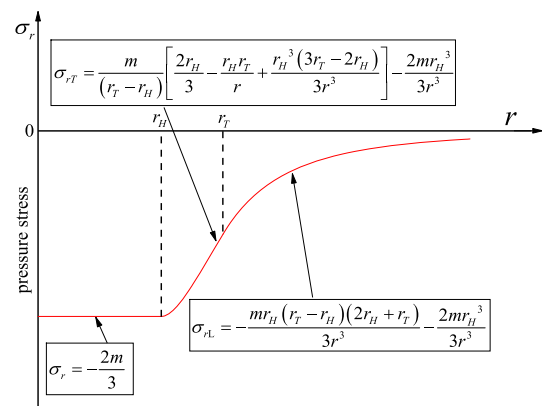


Fig. 6 Variation of σ_r with r for case III

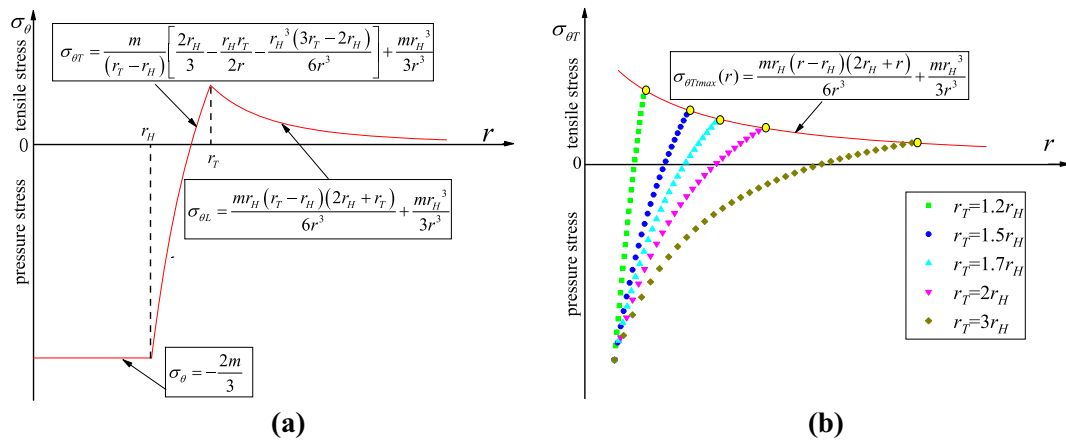


Fig. 7 Variation of **a** σ_θ with radius r and **b** $\sigma_{\theta Tmax}$ with radius r for different r_T/r_H and $\sigma_{\theta Tmax}$ for Case III

distributed, and that in the T zone and the L zone decrease with increasing radius. The maximum compressive stress occurs in the H zone, and its value is unrelated to r , r_H , and r_T .

3.3.2 Variation of circumferential stress for Case III

As shown in Fig. 7a, the tangential stress in the H zone is uniformly distributed and acts as a compressive stress. A maximum compressive stress of $-2m/3$ acts in the H zone which is independent of r , r_H , and r_T . In contrast, the tangential stress in the T zone changes from compressive to tensile with increasing radius. The maximum tensile stress occurs at the outer boundary of the T zone, with a magnitude of:

$$\sigma_{\theta Tmax}(r) = \frac{mr_H(r-r_H)(2r_H+r)}{6r^3} + \frac{mr_H^3}{3r^3} \quad (29)$$

and decreases with increasing r_T . Also as shown in Fig. 7b, $\sigma_{\theta Tmax}$ also decreases with increasing radius r_T/r_H .

3.4 Case IV-general case—spectrum of thermal expansion or temperature gradient induced stress effects— $n/m = k$

In this section, the general case is defined where thermal expansion and temperature gradient induced stresses co-dominate the microwave fracturing process. A parameter, k , is defined as the ratio of the two coupling coefficients ($n/m = k$) and the model can be simplified to:

$$\sigma_r = \begin{cases} -\frac{2m}{3} & (0 < r \leq r_H) \\ \frac{km}{(r_T-r_H)} \left[\frac{2r_H}{3} - \frac{r_H r_T}{r} + \frac{r_H^3(3r_T-2r_H)}{6r^3} \right] - \frac{2mr_H^3}{3r^3} & (r_H \leq r \leq r_T) \\ -\frac{km}{3(1-\mu)} \frac{r_H(r_T-r_H)(2r_H+r_T)}{r^3} - \frac{2mr_H^3}{3r^3} & (r_T \leq r \leq r_L) \end{cases} \quad (30)$$

$$\sigma_\theta = \begin{cases} -\frac{2m}{3} & (0 < r \leq r_H) \\ \frac{km}{(r_T-r_H)} \left[\frac{2r_H}{3} - \frac{r_H r_T}{2r} + \frac{r_H^3(3r_T-2r_H)}{6r^3} \right] + \frac{mr_H^3}{3r^3} & (r_H \leq r \leq r_T) \\ \frac{kmr_H(r_T-r_H)(2r_H+r_T)}{6r^3} + \frac{mr_H^3}{3r^3} & (r_T \leq r \leq r_L) \end{cases} \quad (31)$$

As shown in Eqs. (30) and (31), $\sigma_{rH} = \sigma_{\theta H}$ and this relationship is independent of k —consistent with first three cases. From the three aforementioned cases, the maximum tensile stress and the maximum compressive stress are usually present in the T zone. Therefore, the stress distribution and evolution of the maximum stress in the T zone are illustrated in the following.

3.4.1 Variation of radial stress for Case IV

As shown in Fig. 8a, the relationship between the radial compressive stress in the T zone changes from convex upward to concave upward with increasing k . For $0 \leq k < 1$, the maximum compressive stress is always found at $r = r_H$ and for $k \geq 1$, the location of the maximum value of compressive stress can be obtained as:

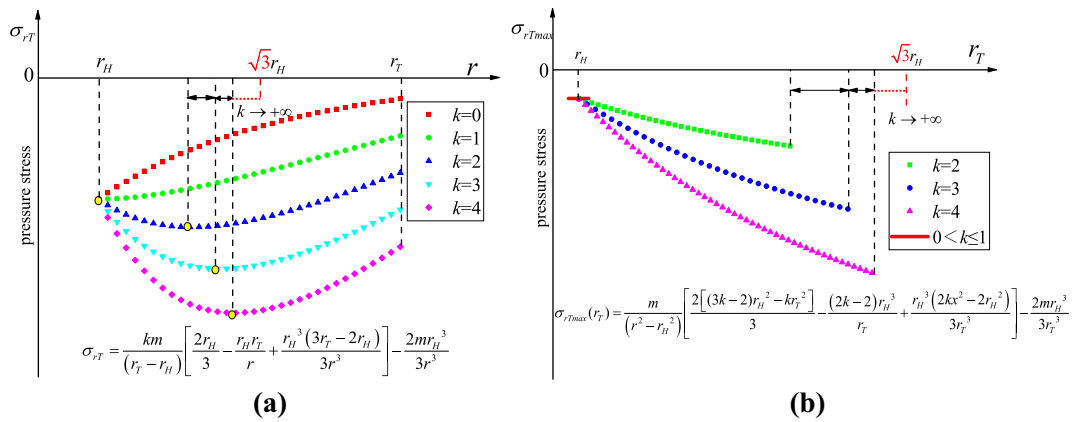


Fig. 8 Variation of **a** σ_{rT} and **b** σ_{rTmax} with r for different values of k

$$r_{rTmax} = r_H \sqrt{\frac{(3k - 2)r_T - (2k - 2)r_H}{kr_T}} \tag{32}$$

when $r_T \rightarrow \infty$, $r_{rTmax} = \sqrt{\frac{3k-2}{k}}r_H$. The position of the maximum stress gradually shifts to $r = \sqrt{3}r_H$ as k increases ($k \rightarrow \infty$). When $k \rightarrow \infty$ and $r_T \rightarrow \infty$, the distribution of radial compressive stress in the T zone is similar to that obtained for Case II.

Furthermore, we can obtain the maximum value of σ_{rT} :

$$\sigma_{rTmax}(r_T) = \frac{m}{(r_T^2 - r_H^2)} \left[\frac{2[(3k - 2) - kr_T^2]}{3} - \frac{(2k - 2)r_H^3}{r_T} + \frac{r_H^3(2kx^2 - 2r_H^2)}{3r_T^3} \right] - \frac{2mr_H^3}{3r_T^3} \tag{33}$$

As shown in Fig. 8b, the magnitude and location of the maximum compressive stress (σ_{rTmax}) remains unchanged for $0 \leq k \leq 1$; and for $k > 1$, the maximum value of σ_{rTmax} increases with r and its position shifts outwards and approaches $r = \sqrt{3}r_H$ when $k \rightarrow \infty$ and $r_T \rightarrow \infty$. The distribution of radial compressive stress in the T zone is similar to that obtained for Case II.

3.4.2 Variation of circumferential stress for Case IV

As shown in Fig. 9a, the tangential stress first decreases then increases with radius when the value of k increases. Therefore a threshold value exist for k : below the threshold value, the tangential stress is

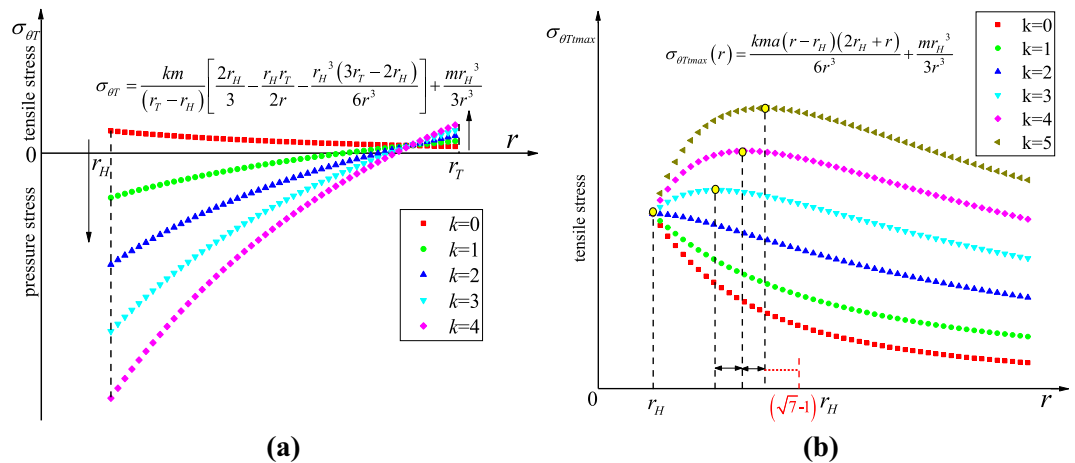


Fig. 9 Variation of **a** $\sigma_{\theta T}$ and **b** $\sigma_{\theta Tmax}$ with r for different values of k

tensile in the T zone while above this value it changes to compressive stress to a tensile stress.

The threshold value can be obtained through the derivative with respect to r :

$$k_H = \frac{2(r_T^3 - r_H^3)}{r_H^2 r_T + r_H r_T^2 - 2r_H^3 + 6r_T^3} \quad (34)$$

When k is below this value, the maximum tensile stress occurs at $r = r_H$ and is of magnitude:

$$\sigma_{\theta T_{max}} = \sigma_{\theta T}(r_H) = -km + \frac{m}{3} \quad (35)$$

When k is above this magnitude, the maximum tensile stress occurs at $r = r_T$ and we have:

$$\sigma_{\theta T_{max}}(r) = \frac{kmr_H(r - r_H)(2r_H + r)}{6r^3} + \frac{mr_H^3}{3r^3} \quad (36)$$

We can also obtain the position of the maximum value of $\sigma_{\theta T_{max}}(r)$ as:

$$r_{\theta T_{max}} = r_T = \frac{r_H \sqrt{7k^2 - 6k}}{k} - r_H \quad (37)$$

when $k \rightarrow \infty$, $r_{\theta T_{max}} = (\sqrt{7} - 1)r_H$.

As shown in Fig. 9b, the maximum tensile stress ($\sigma_{\theta T_{max}}(r)$) first increases then decreases with increasing r and the position of the maximum tangential stress ($\sigma_{\theta T_{max}}(r)$) approaches $r = (\sqrt{7} - 1)r_H$ when $k \rightarrow \infty$. The distribution of radial compressive stress within the T zone is similar to that for Case II.

4 Experimental validation

We validate this model against observations for microwave heating in rock. Two samples of ore were microwave irradiated to validate our theoretical model and comparisons with other experimental observations conducted.

4.1 Sample preparation

Granulite ore samples were collected from the Danyin Mining and Metallurgy Company in Fengcheng City, Liaoning, north-eastern China. Two standard cylindrical plugs were prepared with a dimension of $\phi 50 \times 25$ mm. The two plugs were cored from the same block of ore to maintain consistency between samples and to reduce the impact of large-scale heterogeneity on the test results.

4.2 Experimental method

A multi-mode microwave system operating at a frequency of 2.45 GHz was used to irradiate the samples. In the test, microwave irradiation was applied at 3 kW for 3 min. The samples were located in the same position within the microwave oven in all tests. After the completion of microwave heating, the distribution of surface temperature of samples was measured via infrared thermal imaging; the samples were then removed from the oven enclosure and cooled to room temperature in air.

The measured surface temperature on the samples was non-uniformly distributed as shown in Fig. 10—resulting in a temperature gradient within the plug—and defining the position and extent an H zone. The radial macroscopic fractures developed and were centered on the H Zone with no tangential macroscopic fracture apparent. A pyrite-rich zone was present in the H zone with strong absorptive capacity for the microwave radiation. This zone was heated rapidly and was the remnant area of high temperature.

Based on comparisons of the post-heating distribution of surface temperature together with morphological characteristics, the samples were wire-cut into prismatic sub-samples ($10 \times 10 \times 20$ mm) with a height to diameter ratio of 2:1 (Fig. 11). A computer-controlled loading machine was used to measure uniaxial compressive strength (UCS) under loading at a constant rate of rate of 0.05 mm/min.

4.3 Comparison with model results

The elastic modulus of each element degrades monotonically as damage evolves, with the elastic modulus of the damaged material typically expressed as (Cui et al. 2019):

$$D_E = 1 - \frac{E_i}{E} \quad (38)$$

where D_E refers to a damage variable defined as a function of the change in elastic modulus (plotted in Fig. 12b); E_i and E denote the mean elastic modulus of rocks in different zones both after and before microwave irradiation.

Similarly, a strength reduction ratio (Fig. 12a) may be defined as:

Fig. 10 Surface morphologies and distribution of surface temperatures of plugs immediately after microwave treatment (the blue dashed lines define the boundary of the T zone and the white dashed lines the boundary of the H zone)

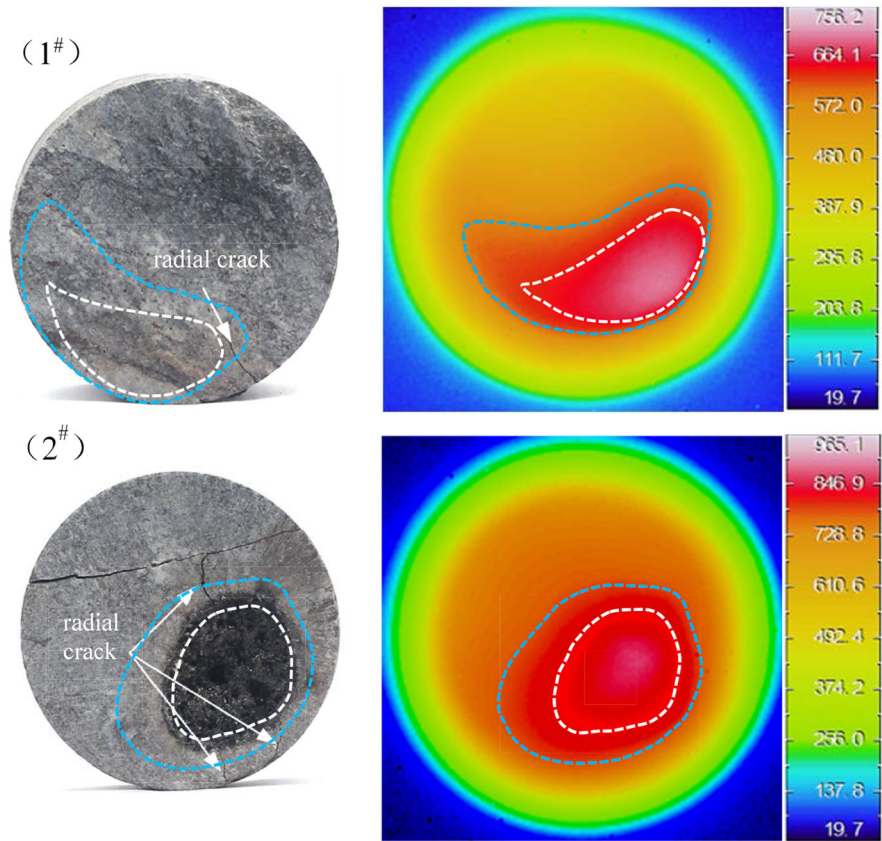
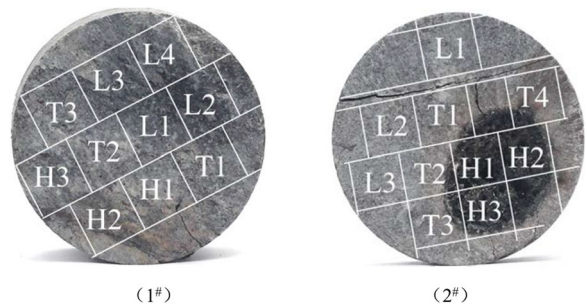


Fig. 11 Sub-sectioned samples



$$\eta = 1 - \frac{\sigma'_c}{\sigma_c} \quad (39)$$

in which σ_c and σ'_c represent the UCS both before then after microwave irradiation.

The results for both the damage variable and strength reduction are shown in Fig. 12. The trend in the damage variable is consistent with that of the reduction in UCS (both decrease radially outwards from the H zone). The damage variables for all samples exceed 0.5 and the strength reduction of all

samples exceed 0.4. All samples generally exhibit a high degree of damage depending on applied microwave power, irradiation duration, and dimension of samples as tested, as well as sustaining increasing damage with closeness to the H zone.

Based on the characteristics of the stress distribution from our prior mechanical model, it is apparent that the radial cracks induced by tensile failure are most likely to be generated by heating, as the tensile strength of the rock is significantly lower than its compressive strength. This fits with observations from

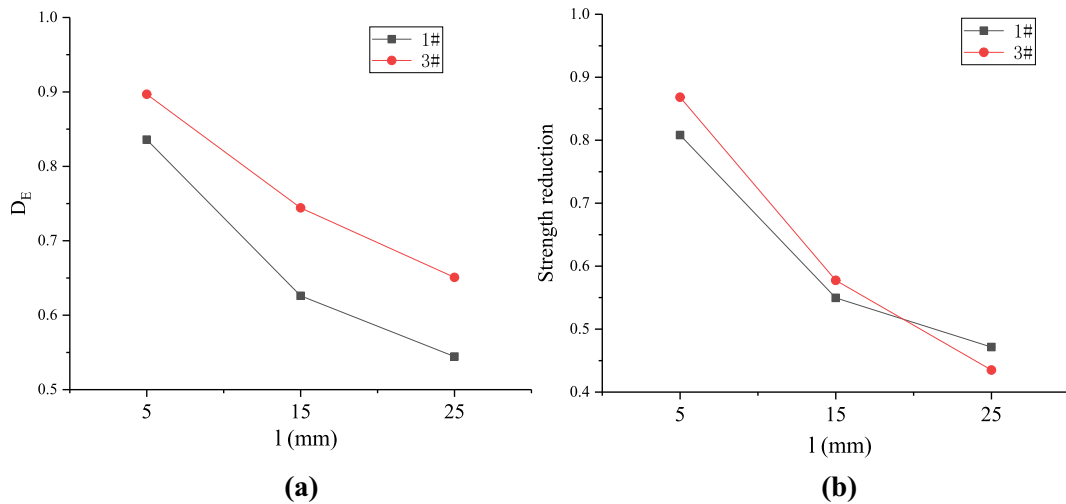


Figure 12 **a** Strength reduction and **b** damage variable in samples 1# and 2#. Length, l , represents the distance from the center of the H zone. Lengths of $l = 5$ mm, 15 mm and 25 mm

are in the H Zone (0–10 mm), T Zone (10–20 mm) and L Zone (20–30 mm), respectively.

the tests where several radial fractures developed around the H zone of the test specimens, as shown in Fig. 10.

As mentioned previously, the non-uniform distribution of temperature results from the heterogeneous distribution of minerals within the sample, categorized as Case IV in Sect. 3.4. The maximum tensile stress would appear at a radius $r = r_T$ for $r_T \leq (\sqrt{7} - 1)r_H$, with its magnitude decreasing with increasing radius together with the damage variable. Conversely, the maximum compressive stress occurs in the area near the H zone and withing the range $r_H < r < \sqrt{3}r_H$, and its stress magnitude decreasing with increasing radius. For this particular experiment, the radius of the H zone is ~ 5 –10 mm, therefore the maximum tensile stress would appear at radii in the range $5 \text{ mm} \leq l \leq 16$ mm and the maximum compressive stress would appear in the range $5 \text{ mm} \leq l < 17.4$ mm. In such conditions, the prismatic sub-samples at $l = 25$ mm are beyond the range of maximum tensile stress and thus returns the smallest damage variable—consistent with the UCS test results.

4.4 Other experimental observations

Hartlieb et al. (2016) conducted a microwave irradiation test on a rock (granite) surface using an open high power microwave radiation device and measured surface temperatures by infrared thermometer.

Following microwave irradiation, a high temperature zone appeared with a diameter of ~ 10 cm, with the remainder of the sample remaining in the low temperature zone, and only a small transition zone separating the low and high temperature zones, as shown in Fig. 13. Several radial fractures developed on the rock surface and expanded in the T and L zones without crossing the H zone.

This granite can be treated as a quasi-homogeneous material impacted by beam-focused irradiation developing an uneven temperature distribution—rather than resulting from rock heterogeneity. Therefore, this case can be categorized into that of Case III of Sect. 3.3. Based on our prior model, the tensile stress appears in what would be classified as the T and L zone with compressive stresses in the H zone. Furthermore the tensile strength is much smaller than the compressive stress, favoring the first development of tensile stress-induced fractures.

Similarly, Lu et al. (2019) used an open-type microwave-induced fracturing apparatus (OMWFA) to irradiate and heat a basalt sample. The results at a power of 3kw and for irradiation times of 1 min, 2 min and 3 min are illustrated in Fig. 14 with the white rectangles representing the location of the waveguide. As apparent in the figure, radial fractures appeared after one minute of microwave irradiation, with these outside the waveguide. The radial fractures extend both outward from, and inward to, the waveguide with

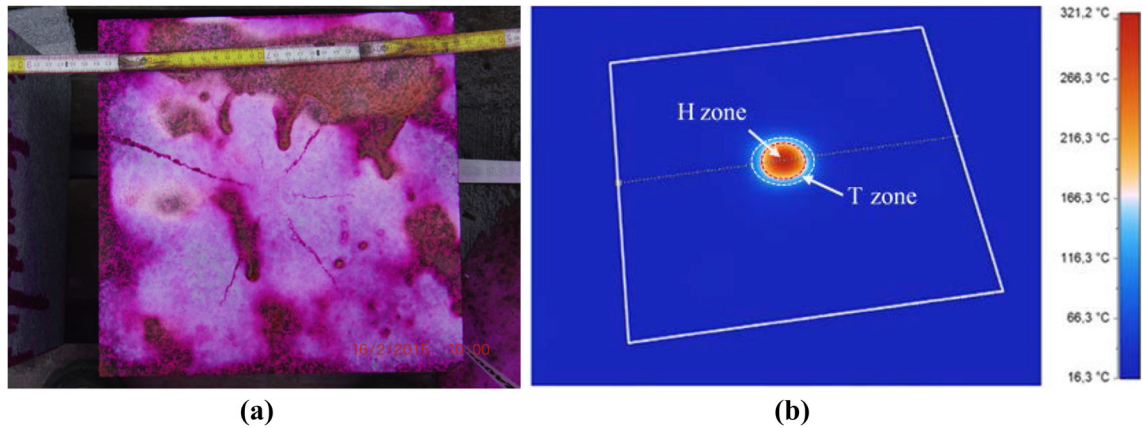


Figure 13 **a** Fracture network developed in granite after 30 s of microwave irradiation at 17.5 kW. The sample was treated with a penetrative spray to improve visibility of the cracks. **b** Surface

temperature after 30 s microwave irradiation of granite at 17.5 kW (Hartlieb et al. 2016).

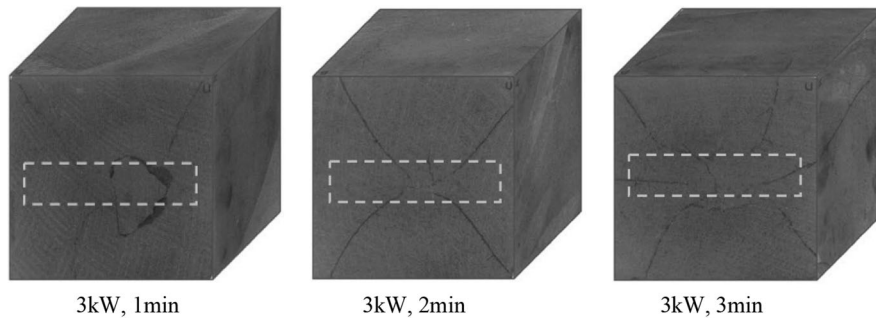


Fig. 14 Extension of fractures on the surfaces of a 100 mm edge-dimension cubic sample. Fractures on the microwave irradiated surface propagate outwards from the approximate

center of the sample; with increasing irradiation time, the cracks progressively extend within the cube and away from the irradiated surface (Lu et al. 2019)

an increase in the duration of irradiation: a radial fracture appeared in the waveguide area after 2 min of microwave irradiation and this became more significant at 3 min.

Basalt may also be regarded as a quasi-homogeneous medium (Meisels et al. 2015) with a near-uniform distribution of thermophysical characteristics throughout. Therefore, this experiment belongs to Case III in our classification in which the maximum tensile stress occurs at the outer boundary of the T Zone, a certain distance from the H zone. With increasing irradiation time, the tensile stress in both the T and L zones increases, leading to an expansion of the radial fracture. Once the compressive stresses in the H and T zones exceed the compressive strength, the circumferential fracture will appear.

5 Discussion

The previous has detailed a physics-based model describing the likely distribution of fracturing that will develop as a result of non-uniform heating within irradiated samples. We discuss the findings and limitations of this work in the following.

5.1 Distribution of stress and induced fractures

5.1.1 Radial stress

Based on the previous analysis (Sect. 3.4, $n/m = k$), the radial stresses that develop within the different zones are all compressive (or neutral as $r \rightarrow \infty$). For the case $0 \leq k \leq 1$, the maximum induced radial stress occurs in the H zone and is uniformly distributed in that zone; For the case $k > 1$, (1) the compressive

stress first increases then decreases with increasing radius and its maximum occurs at $r=r_H\sqrt{\frac{(3k-2)r_T-(2k-2)r_H}{kr_T}}$; (2) the compressive stress increases with increasing k when the values of m, r_H, r_T remain unchanged; and (3) the maximum compressive stress increases with the extension of the T zone and the location of the maximum value approaches $r=\sqrt{3}r_H$, again when m, r_H, r_T are retained unchanged.

5.1.2 Circumferential stress

Both tensile and compressive stresses develop around the circumference of these zones, with the former (tension) occurring in both the T and L zones and the latter (compression) occurring in both the H and T zones. The compressive stress decreases with increasing radius becomes tensile stress inside the T zone. The relationship between compressive stress and k is first investigated. For the case $0 \leq k \leq 1$, the maximum circumferential stress occurs within the H zone and is uniformly distributed in that zone. For $k > 1$: (1) the maximum compressive stress is located at the inner boundary of the T zone; and (2) the maximum compressive stress increases with k for constant m, r_H, r_T .

The relationship between tensile stress and k may also be analyzed. For the case $0 \leq k \leq \frac{2(r_T^3-r_H^3)}{r_H^2r_T+r_Hr_T^2-2r_H^3+6r_T^3}$: (1) the maximum tensile stress occurs at the inner boundary of the T zone; and (2) the tensile stress decreases with increasing k outside the H zone with the maximum value increasing with increasing k for constant m, r_H, r_T . For $k > \frac{2(r_T^3-r_H^3)}{r_H^2r_T+r_Hr_T^2-2r_H^3+6r_T^3}$: (1) the value of $\sigma_{\theta Tmax}$ first increases then decreases with the areal expansion of the T zone for constant m, r_H, r_T ; and (2) the maximum value of $\sigma_{\theta Tmax}$ also varies with a maximum occurring at the outer boundary of the T zone ($r = r_T = \frac{r_H\sqrt{7k^2-6k}}{k} - r_H$).

5.1.3 Fracture propagation

The maximum magnitude of compressive stress occurs in the range $0 \leq r < \sqrt{3}r_H$ and the maximum tensile stress is found within the range $r_H < r < (\sqrt{7} - 1)r_H$. The exact locations of these stresses is determined by the coupling coefficients

(m and n) and the dimensions of the three zones. Damage evolves once the compressive or tensile stresses exceed strength.

Therefore, we conclude that: (1) circumferential fracturing will occur in the L zone, induced by the compressive stress and both circumferential and radial fractures will occur within the H and T zones; that (2) tensile stress will induce radial fractures in both the T and L zones, and that the location of the fracturing position will be in the range $r_H \leq r < (\sqrt{7} - 1)r_H$ or at a certain position outside the H zone; and (3) fractures will extend both inward and outward during continued microwave irradiation.

5.2 Temperature-dependent parameters and mineral transitions

Mineral phase transition and melting both potentially impact the microwave heating induced fracturing process. Quartz, for example will transition from α to β phase at a temperature of 573 °C (Vidana et al. 2021). During this transition process, the heat capacity (Abdulagatova et al. 2020), the thermal expansion coefficient and Young’s modulus change dramatically (Zhao et al. 2017). In addition, pyrite may melt during microwave heating (Lu et al. 2017), if the temperature change is sufficient, resulting an increase in mineral volume.

The temperature in the H zone continues to increase during the microwave irradiation process. The thermal diffusion coefficient (Hartlieb et al. 2016) and Young’s modulus (Chen et al. 2014; Ahmed et al. 2018; Peng and Redfern 2013) decrease with increased temperature, while the thermal expansion coefficient (Meisels et al. 2015; Wang and Djordjevic 2014; Toifl et al. 2016) increases. These variations in thermo-physical parameters impact the values of the scaling constants n and m . Apparent from Eqs. (19) and (20), the value of n increases with increasing temperature. In contrast, the impact of increasing temperature on the value of m is much more complicated. In most cases, the value of m increases with increasing temperature. Only in the case where the reduction of the value of m induced by a decreased Young’s modulus is larger than the increment caused by the increasing thermal diffusion coefficient and temperature, does the value of m decrease. The increases in m and n increase the maximum magnitudes of induced

tensile and compressive stresses, thereby potentially increasing damage. Within the prior model, the relationship between the relevant parameters in the coupling coefficients and temperature are readily established to analyze the influence of mineral phase transition, melting and other phenomena on the distribution of thermal stress, and therefore enable predict of the locations and severity of damage.

5.3 Limitations

Rocks are typically highly heterogeneous. In addition to heterogeneous distributions of minerals, they contain cracks, pores, grain boundary defects and cleavage—one of which are included in the current model. In addition, the heated region is assumed spherical and thereby does not consider the influence of an irregular model geometry on induced thermal stress. For example, because of the spherically symmetrical nature of the geometric model, the effect of additional induced shear stress is neglected. Furthermore, this study assumes that the microwave intensity in the high temperature region is uniform, with the model using an average magnitude of microwave intensity over the high microwave intensity region—all of which may be different from the actual situation at sample and macroscopic scales. These are all issues to be considered in future research.

6 Conclusions

To investigate the impact of microwave radiation induced temperature and thermal stress, a mechanic model comprising nested spherical zones has been developed. With this model, the thermal stress distribution is defined, enabling microwave heating induced fracture propagation to be rigorously analyzed. Resulting model results are verified by microwave irradiation experiments. The following conclusions can be drawn:

(1) In the model, temperature gradient coupling coefficient (n) and thermal expansion coupling coefficient (m) are defined. The thermal stresses develop as a result of two superposed processes: constrained thermal expansion of the central heated core and stresses resulting from the temperature gradient within the transitional

zone. As a result of this decomposition, the stress distribution is shown to be uniquely related to both the thermal stress coupling coefficients and the geometric dimensions of the three zones.

- (2) The relationship between n and m plays a significant role in the location of the maximum compressive/tensile stress and the thermal stress distribution. For the radial stress, acting as a compressive stress in all the three zones, the maximum stress occurs in the high temperature zone (H zone) or transitional zone (T zone). For the circumferential stress, acting as a compressive stress in the H zone, a tensile stress in the low temperature zones (L zones), and in the T zone is tensile stress or coexistence of tensile stress and compressive stress. The maximum compressive stress occurs in the H zone or at the inner boundary of the T zone. The maximum tensile stress occurs at the inner or the outer boundary of the T zone.
- (3) The relationship between the radius of H zone (r_H) and the radius of T zone (r_T) plays a significant role in the variation of maximum compressive/tensile stress. For the radial stress, when the maximum compressive stress appears at the inner boundary of T zone, $\sigma_{\theta Tmax}$ increases with the increase of the ratio of r_H to r_T . For the circumferential stress, when the maximum tensile stress appears at the inner boundary of T zone, $\sigma_{\theta Tmax}$ decreases with the increase of the ratio of r_H to r_T ; when the maximum tensile stress appears at the outer boundary of T zone, with the increase of the ratio of r_H to r_T , $\sigma_{\theta Tmax}$ first increases and then decreases.
- (4) The results show that radial cracks are more likely to develop than circumferential cracks. The location of the initial fracture is most likely located at radius $r_H \leq r < (\sqrt{7} - 1)r_H$, that is in the inner boundary of T zone, or a small distance from H zone. This model provides a theoretical and rigorous approach to obtain the thermal stresses induced by a non-uniform temperature field under microwave radiation—enabling bounds to be placed on expected locations and density of fracturing to develop within irradiated media.

Acknowledgements The work presented in this paper is supported by the National Key Research and Development Program of China (Grant No. 2018YFC0604601), Revitalization Talent Program (XLYC1805008), National Natural Science Foundation of China (Grant No. 51974059), the Fundamental Research Funds for the Central Universities (Grant Nos. 02070022119023, N180115010), the 111 Project (B17009) which are greatly appreciated.

Declarations

Conflict of interest The authors declare no competing interests.

Appendix 1

Pressure, P , applied to the exterior surface of a solid sphere

Based on elastic mechanics, if the outer part of the solid sphere is subjected to uniformly distributed pressure P , the three principal stresses at any point in the sphere are all equal to $-P$, that is:

$$\sigma_r = \sigma_\theta = -P \tag{40}$$

where σ_r and σ_θ refer to radial and tangential stresses, respectively.

Pressure, P , applied to the interior surface of a hollow sphere

For a hollow sphere with the inner radius of r_1 , outer radius of r_2 and $r_2 \gg r_1$, subjected to uniformly distributed inner pressure P , the radial and tangential stresses at any point in the sphere are separately expressed as follows:

$$\sigma_r = -\frac{Pr_1^3}{r^3} \tag{41}$$

$$\sigma_\theta = \frac{Pr_1^3}{2r^3} \tag{42}$$

where σ_r and σ_θ refer to radial and circumferential stresses, respectively.

Pressure, P , applied to the exterior surface of a hollow sphere

When the outer boundary of the hollow sphere is under the action of uniformly distributed pressure P , the

radial and tangential stresses at any point in the sphere are given by:

$$\sigma_r = -\frac{Pr_2^3(r^3 - r_1^3)}{r^3(r_2^3 - r_1^3)} \tag{43}$$

$$\sigma_\theta = -\frac{Pr_2^3(r_1^3 + 2r^3)}{2r^3(r_2^3 - r_1^3)} \tag{44}$$

Temperature gradient induced stress within a hollow sphere

The temperature gradient induced thermal stress can be treated as the case where a hollow sphere is under free expansion with the temperature variations on the inner and outer boundary are ΔT and zero. Li et al. (2003) deduced the equations for gradient induced thermal stress generated on a hollow sphere with inner diameter r_1 and outer diameter r_2 :

$$\sigma_r = \frac{\alpha E \Delta T}{1 - \mu} \frac{r_1 r_2}{r_2^3 - r_1^3} \left[r_1 + r_2 - \frac{1}{r} (r_1^2 + r_1 r_2 + r_2^2) + \frac{r_1^2 r_2^2}{r^3} \right] \tag{45}$$

$$\sigma_\theta = \frac{\alpha E \Delta T}{1 - \mu} \frac{r_1 r_2}{r_2^3 - r_1^3} \left[r_1 + r_2 - \frac{1}{2r} (r_1^2 + r_1 r_2 + r_2^2) - \frac{r_1^2 r_2^2}{2r^3} \right] \tag{46}$$

Relationship between stress and strain in the thermal expansion of a sphere

According to Hooke’s law, the relationship between strain and stress at any point in a hollow sphere deformed by thermal expansion are given by:

$$\varepsilon_\theta = \frac{1}{E} [\sigma_\theta - \mu(\sigma_\theta + \sigma_r)] + \alpha t \tag{47}$$

where ε_r , ε_θ , E , μ , α and t refer to radial strain, circumferential strain, Young’s moduli, Poisson’s ratios, the coefficients of thermal expansion and temperature.

The geometric equations satisfying the spherical symmetry condition are expressed:

$$\varepsilon_\theta = \frac{u_r}{r} \tag{48}$$

where u_r , r refer to radial displacement and radius.

Solving analytical solutions

According to Eqs. (43), (44), the radial and circumferential stresses produced by $P_{To(T-L)}$ at the outer boundary of T zone are given by ($r_1 = r_H, r = r_2 = r_T$):

$$\sigma_{rTo(T-L)} = -P_{To(T-L)} \tag{49}$$

$$\sigma_{\theta To(T-L)} = -\frac{2r_T^3 + r_H^3}{2r^3(r_T^3 - r_H^3)} P_{To(T-L)} \tag{50}$$

According to Eqs. (47)–(50), the radial displacement produced by $P_{To(T-L)}$ at the outer boundary of T zone are given by:

$$u_{To(T-L)} = -\frac{r_T^3(1 + \mu)P_{To(T-L)}}{E} \left(\frac{2r_T^3 + r_H^3}{2(r_T^3 - r_H^3)} - \frac{\mu}{1 - \mu} \right) \tag{51}$$

Similarly, according to Eqs. (45)–(48), the radial displacement produced by temperature gradient at the outer boundary of T zone and the radial displacement produced by $P_{Li(T-L)}$ at the inner boundary of L zone are given by ($r_1 = r_H, r = r_2 = r_T$):

$$u_{To(g)} = \frac{\alpha T_H r_H^3 (r_T^3 - r_H^3) (2r_H^3 + r_T^3)}{2(r_T^3 - r_H^3)} \tag{52}$$

$$u_{Li(T-L)} = -\frac{r_T^3(1 + \mu)P_{Li(T-L)}}{2E} \tag{53}$$

According to Eqs. (12), (51)–(53) and $P_{To(T-L)} = P_{Li(T-L)}, P_{To(T-L)}$ and $P_{Li(T-L)}$ are given by:

$$P_{To(T-L)} = P_{Li(T-L)} = \frac{\alpha_{T\&L} E_{T\&L} T_H r_H (r_T - r_H) (2r_H + r_T)}{3(1 - \mu_{T\&L}) r_T^3} \tag{54}$$

According to Eqs. (43)–(48), (54), (10), we obtain the displacement on the inner boundary of the T&L Zone induced by the temperature gradient in the T Zone and constraint of the L Zone as zero:

$$u_{T\&Li(g\&T-L)} = u_{Ti(g)} + u_{Ti(T-L)} = 0 \tag{55}$$

Furthermore $P_{Ho(T\&L-H)}$ and $P_{Ti(T\&L-H)}$ are induced by the displacement on the inner boundary of the T&L Zone ($u_{T\&Li(g\&T-L)}$), therefore we have:

$$P_{Ho(T\&L-H)} = P_{Li(T\&L-H)} = 0 \tag{56}$$

The compressive stress induced by the thermal expansion of the H zone against the L&T Zone ($P_{H-T\&L}$) can be treated as an inner pressure on the hollow

sphere with inner radius of r_H and outer radius r_L . According to Eqs. (5), (6), (9), (14), (15), (40)–(42) and (47)–(48), $P_{Ho(H-T\&L)}$ and $P_{Ti(H-T\&L)}$ and can be written as:

$$P_{Ho(H-L\&T)} = P_{Ti(H-L\&T)} = \frac{2\alpha_H E_H E_{T\&L} T_H}{(1 + \mu_{T\&L}) E_H + 2(1 - 2\mu_H) E_{T\&L}} \tag{57}$$

According to Eqs. (41), (42), (54), the radial and circumferential stresses produced by $P_{Li(T-L)}$ in the L zone are given by:

$$\sigma_{rL(T-L)} = -\frac{\alpha_{T\&L} E_{T\&L} T_H r_H (r_T - r_H) (2r_H + r_T)}{3(1 - \mu_{T\&L}) r^3} \tag{58}$$

$$\sigma_{\theta L(T-L)} = \frac{\alpha_{T\&L} E_{T\&L} T_H r_H (r_T - r_H) (2r_H + r_T)}{6(1 - \mu_{T\&L}) r^3} \tag{59}$$

According to Eqs. (43), (44), (54), the radial and circumferential stresses produced by $P_{To(T-L)}$ in the T zone are given by:

$$\sigma_{rT(T-L)} = -\frac{\alpha_{T\&L} E_{T\&L} T_H r_H (r_T - r_H) (2r_H + r_T)}{3(1 - \mu_{T\&L}) r^3 (r_T^3 - r_H^3)} \tag{60}$$

$$\sigma_{\theta T(T-L)} = -\frac{\alpha_{T\&L} E_{T\&L} T_H r_H (r_T - r_H) (2r_H + r_T) (r_H^3 + r^3)}{6(1 - \mu_{T\&L}) r^3 (r_T^3 - r_H^3)} \tag{61}$$

According to Eqs. (40), (57), the radial and circumferential stresses produced by $P_{Ho(H-T\&L)}$ in the H zone are given by:

$$\sigma_{rH(H-L\&T)} = \sigma_{\theta H(H-L\&T)} = \frac{2\alpha_H E_H E_{T\&L} T_H}{(1 + \mu_{T\&L}) E_H + 2(1 - 2\mu_H) E_{T\&L}} \tag{62}$$

According to Eqs. (41), (42), (57), the radial and circumferential stresses produced by $P_{T\&Li(H-T\&L)}$ in the T&L zone are given by:

$$\sigma_{rL\&T(H-L\&T)} = -\frac{2\alpha_H E_H E_{T\&L} T_H r_H^3}{(1 + \mu_{T\&L}) E_H + 2(1 - 2\mu_H) E_{T\&L} r^3} \tag{63}$$

$$\sigma_{\theta L \& T(H-L \& T)} = \frac{\alpha_H E_H E_{T \& L} T_H}{(1 + \mu_{T \& L}) E_H + 2(1 - 2\mu_H) E_{T \& L}} \frac{r_H^3}{r^3} \quad (64)$$

References

- Abdulagatov IM (2020) Temperature effect on thermal-diffusivity and heat-capacity and derived values of thermal-conductivity of reservoir rock materials. *Geomech Geophys Geoenergy Georesour* 6:8. <https://doi.org/10.1007/s40948-019-00131-2>
- Ahmed MF, Waqas U, Arshad M, Rogers JD (2018) Effect of heat treatment on dynamic properties of selected rock types taken from the Salt Range in Pakistan. *Arab J Geosci* 11:728. <https://doi.org/10.1007/s12517-018-4058-5>
- Ali AY, Bradshaw SM (2009) Quantifying damage around grain boundaries in microwave treated ores. *Chem Eng Process* 48:1566–1573. <https://doi.org/10.1016/j.cep.2009.09.001>
- Amankwah RK, Pickles CA (2009) Microwave roasting of a carbonaceous sulphidic gold concentrate. *Miner Eng* 22:1095–1101. <https://doi.org/10.1016/j.mineng.2009.02.012>
- Buttress AJ, Katrib J, Jones DA, Batchelor AR, Craig DA, Royal TA, Dodds C, Kingman SW (2017) Towards large scale microwave treatment of ores: Part 1—basis of design, construction and commissioning. *Miner Eng* 109:169–183. <https://doi.org/10.1016/j.mineng.2017.03.006>
- Charikinya E, Bradshaw S, Becker M (2015) Characterising and quantifying microwave induced damage in coarse sphalerite ore particles. *Miner Eng* 82:14–24. <https://doi.org/10.1016/j.mineng.2015.07.020>
- Chen YL, Ni J, Jiang LH, Liu ML, Wang P, Azzam R (2014) Experimental study on mechanical properties of granite after freeze–thaw cycling. *Environ Earth Sci* 71:3349–3354. <https://doi.org/10.1007/s12665-013-2725-0>
- Cui GL, Wei J, Feng XT, Liu JS, Elsworth D, Chen TY, Xiong W (2019) Preliminary study on the feasibility of co-exploitation of coal and uranium. *Int J Rock Mech Min Sci* 123:104098. <https://doi.org/10.1016/j.ijrmms.2019.104098>
- Guo SH, Chen G, Peng JH, Chen J, Li DB, Liu LJ (2011) Microwave assisted grinding of ilmenite ore. *T Nonferr Metal Soc* 21:2122–2126. [https://doi.org/10.1016/S1003-6326\(11\)60983-7](https://doi.org/10.1016/S1003-6326(11)60983-7)
- Hartlieb P, Grafe B (2017) Experimental study on microwave assisted hard rock cutting of granite. *Berg Huettenmaenn Monatsh* 162:77–81. <https://doi.org/10.1007/s00501-016-0569-0>
- Hartlieb P, Leindl M, Kuchar F, Antretter T, Moser P (2012) Damage of basalt induced by microwave irradiation. *Miner Eng* 31:82–89. <https://doi.org/10.1016/j.mineng.2012.01.011>
- Hartlieb P, Toifl M, Kuchar F, Meisels R, Antretter T (2016) Thermo-physical properties of selected hard rocks and their relation to microwave-assisted comminution. *Miner Eng* 91:34–41. <https://doi.org/10.1016/j.mineng.2015.11.008>
- Hartlieb P, Kuchar F, Moser P, Kargl H, Restner U (2018) Reaction of different rock types to low-power (3.2 kW) microwave irradiation in a multimode cavity. *Miner Eng* 118:37–51. <https://doi.org/10.1016/j.mineng.2018.01.003>
- Hong YD, Lin BQ, Li H, Dai HM, Zhu CJ, Yao H (2016) Three-dimensional simulation of microwave heating coal sample with varying parameters. *Appl Therm Eng* 93:1145–1154. <https://doi.org/10.1016/j.applthermaleng.2015.10.041>
- Jones DA, Kingman SW, Whittles DN, Lowndes IS (2005) Understanding microwave assisted breakage. *Miner Eng* 18:659–669. <https://doi.org/10.1016/j.mineng.2004.10.011>
- Jones DA, Kingman SW, Whittles DN, Lowndes IS (2007) The influence of microwave energy delivery method on strength reduction in ore samples. *Chem Eng Process* 46:291–299. <https://doi.org/10.1016/j.cep.2006.06.009>
- Kahraman S, Canpolat AN, Fener MK, Cumhur O (2020) The assessment of the factors affecting the microwave heating of magmatic rocks. *Geomech Geophys Geoenergy Georesour* 6:66. <https://doi.org/10.1007/s40948-020-00197-3>
- Kingman SW, Jackson K, Bradshaw SM, Rowson NA, Greenwood R (2004) An investigation into the influence of microwave treatment on mineral ore comminution. *Powder Technol* 146:176–184. <https://doi.org/10.1016/j.powtec.2004.08.006>
- Li W, Huang BH, Bi ZB (2003) Theoretical analysis and application of thermal stress. Electric Power Press, China
- Li H, Lin BQ, Yang W, Zheng CS, Hong YD, Gao YB, Liu T, Wu SL (2016) Experimental study on the petrophysical variation of different rank coals with microwave treatment. *J Coal Geol* 154–155:82–91. <https://doi.org/10.1016/j.coal.2015.12.010>
- Li H, Shi SL, Lin BQ, Lu JX, Lu Y, Ye Q, Wang Z, Hong YD, Zhu XN (2019a) A fully coupled electromagnetic, heat transfer and multiphase porous media model for microwave heating of coal. *Fuel Process Technol* 189:49–61. <https://doi.org/10.1016/j.fuproc.2019.03.002>
- Li JL, Kaunda RB, Arora S, Hartlieb P, Nelson PP (2019b) Fully-coupled simulations of thermally-induced cracking in pegmatite due to microwave irradiation. *J Rock Mech Geotech* 11:242–250. <https://doi.org/10.1016/j.jrmge.2018.12.007>
- Liu J, Wang JG, Leung CF, Gao F (2018) A fully coupled numerical model for microwave heating enhanced shale gas recovery. *Energies* 11:1608. <https://doi.org/10.3390/en11061608>
- Lu GM, Li YH, Hassani F, Zhang ZXW (2017) The influence of microwave irradiation on thermal properties of main rock-forming minerals. *Appl Therm Eng* 112:1523–1532. <https://doi.org/10.1016/j.applthermaleng.2016.11.015>
- Lu GM, Feng XT, Li YH, Zhang XW (2019) The microwave-induced fracturing of hard rock. *Rock Mech Rock Eng* 52:3017–3032. <https://doi.org/10.1007/s00603-019-01790-z>
- Meisels R, Toifl M, Hartlieb P, Kuchar F, Antretter T (2015) Microwave propagation and absorption and its thermo-mechanical consequences in heterogeneous rocks. *Int J Miner Process* 135:40–51. <https://doi.org/10.1016/j.minpro.2015.01.003>

- Omran M, Fabritius T, Mattila R (2015) Thermally assisted liberation of high phosphorus oolitic iron ore: a comparison between microwave and conventional furnaces. *Powder Technol* 269:7–14. <https://doi.org/10.1016/j.powtec.2014.08.073>
- Peng ZW, Redfern SAT (2013) Mechanical properties of quartz at the α - β phase transition: implications for tectonic and seismic anomalies. *Geochem Geophys Geosyst* 14:18–28. <https://doi.org/10.1029/2012GC004482>
- Pitchai K, Chen J, Birla S, Gonzalez R, Jones D, Subbiah J (2014) A microwave heat transfer model for a rotating multi-component meal in a domestic oven: development and validation. *J Food Eng* 128:60–71. <https://doi.org/10.1016/j.jfoodeng.2013.12.015>
- Rizmanoski V (2011) The effect of microwave pretreatment on impact breakage of copper ore. *Miner Eng* 24:1609–1618. <https://doi.org/10.1016/j.mineng.2011.08.017>
- Satish H, Ouellet J, Raghavan V, Radziszewski P (2006) Investigating microwave assisted rock breakage for possible space mining applications. *Min Technol* 115:34–40. <https://doi.org/10.1179/174328606X101902>
- Toifl M, Meisels R, Hartlieb P, Kuchar F, Antretter T (2016) 3D numerical study on microwave induced stresses in inhomogeneous hard rocks. *Miner Eng* 90:29–42. <https://doi.org/10.1016/j.mineng.2016.01.001>
- Toifl M, Hartlieb P, Meisels R, Antretter T, Kuchar F (2017) Numerical study of the influence of irradiation parameters on the microwave-induced stresses in granite. *Miner Eng* 103–104:78–92. <https://doi.org/10.1016/j.mineng.2016.09.011>
- Vidana PS, Gratchev I, Kong R (2021) Engineering properties of four different rocks after heat treatment. *Geomech Geophys Geoenergy Georesour* 7:16. <https://doi.org/10.1007/s40948-020-00211-8>
- Wang YC, Djordjevic N (2014) Thermal stress FEM analysis of rock with microwave energy. *Int J Mine Process* 130:74–81. <https://doi.org/10.1016/j.minpro.2014.05.012>
- Wen T, Zhao YL, Xiao QH, Ma QL, Kang SC, Li HQ, Song SX (2017) Effect of microwave-assisted heating on chalcopyrite leaching of kinetics, interface temperature and surface energy. *Results Phys* 7:2594–2600. <https://doi.org/10.1016/j.rinp.2017.07.035>
- Yan CZ, Zheng H (2017) A coupled thermo-mechanical model based on the combined finite-discrete element method for simulating thermal cracking of rock. *Int J Rock Mech Min Sci* 91:170–178. <https://doi.org/10.1016/j.ijrmms.2016.11.023>
- Zhang XG, Ranjith PG, Perera MSA, Ranathunga AS, Haque A (2016) Gas transportation and enhanced coalbed methane recovery processes in deep coal seams: a review. *Energy Fuel* 30:8832–8849. <https://doi.org/10.1021/acs.energyfuels.6b01720>
- Zhao YS, Wan ZJ, Feng ZJ, Xu ZH, Liang WG (2017) Evolution of mechanical properties of granite at high temperature and high pressure. *Geomech Geophys Geoenergy Georesour* 3:199–210. <https://doi.org/10.1007/s40948-017-0052-8>
- Zheng YL, Zhang QB, Zhao J (2017) Effect of microwave treatment on thermal and ultrasonic properties of gabbro. *Appl Therm Eng* 127:359–369. <https://doi.org/10.1016/j.applthermaleng.2017.08.060>
- Zheng YL, Zhao XB, Zhao QH, Li JC, Zhang QB (2020) Dielectric properties of hard rock minerals and implications for microwave-assisted rock fracturing. *Geomech Geophys Geoenergy Georesour* 6:22. <https://doi.org/10.1007/s40948-020-00147-z>

Publisher's Note Springer Nature remains neutral with regard to jurisdictional claims in published maps and institutional affiliations.